Research Square

Preprints are preliminary reports that have not undergone peer review.
They should not be considered conclusive, used to inform clinical practice,
or referenced by the media as validated information.

Molecular Targeting of UBR2 in Melasma Using Natural Compounds from Scutellaria baicalensis through Integrated Computational Approaches

Akhtar Veg
Jamia Millia Islamia
Faria Saleem
Jamia Millia Islamia
Romana Ishrat
rishrat@jmi.ac.in

Jamia Millia Islamia

Research Article

Keywords: Melasma, UBR2, Scutellaria baicalensis, Molecular docking, Molecular dynamics simulation

Posted Date: September 18th, 2026

DOI: https://doi.org/10.21203/rs.3.rs-9778230/v1

License: This work is licensed under a Creative Commons Attribution 4.0 International License.
Read Full License

Additional Declarations: No competing interests reported.

Molecular Targeting of UBR2 in Melasma Using Natural Compounds from *Scutellaria baicalensis* through Integrated Computational Approaches

Akhtar Veg[1], Faria Saleem[1], Romana Ishrat[1*]
[1]Centre for Interdisciplinary Research in Basic Sciences, Jamia Millia Islamia, New Delhi 110025, India

Abstract

Melasma is a multifactorial hyperpigmentation disorder with complex molecular mechanisms involving melanogenesis, inflammation, and dermal remodeling. Identification of novel therapeutic targets and safer inhibitors remains a major challenge. Using a combined in-silico approach with molecular docking, ADMET profiling, molecular dynamics simulations, and free energy landscape analysis, a library of 57 phytochemicals from Scutellaria baicalensis was screened. Molecular docking was used to determine binding affinities for each of the compounds, resulting in Ferulic acid and Skullcapflavone II as showed good binding energy. Furthermore, detailed interaction studies demonstrated hydrogen bonding and hydrophobic interactions and pi-interactions in a conserved binding pocket with critical residues. ADMET analyses indicated good pharmacokinetic and safety profile for both compounds, which are compliant with drug-likeness attribute requirements without any toxicity hazards. Molecular dynamics simulations (1000 ns) suggested that upon binding the ligand, higher structural stability of UBR2 was observed as reflected in significant reduction in RMSD, RMSF, radius of gyration and solvent-accessible surface area. The ligand-induced stabilization was additionally validated through increased intra-molecular hydrogen bonding as well as more stabilized elements of secondary structure. Conformational space and free energy landscape analysis showed more compact conformations with deeper minima in ligand-bound systems. Hence, overall, this work provides a strong computational basis for identification of potential UBR2 inhibitors in melasma therapeutics studying two putative molecules Ferulic acid and Skullcapflavone II.

Keywords: Melasma, UBR2, Scutellaria baicalensis, Molecular docking, Molecular dynamics simulation.

*Corresponding author
Romana Ishrat
Centre for Interdisciplinary
Research in Basic Sciences,
Jamia Millia Islamia,
New Delhi 110025, India
Email: rishrat@jmi.ac.in
*Orcid ID: 0000-0001-9744-9047

Introduction

Melasma is a common dermatological disorder whose pathophysiologic mechanisms and management continue to be complex. A deeper knowledge of the cutaneous milieu and disease mechanism/pathways driving melasma will be vital for intervention by current- and future-based therapeutics. Clinically, melasma is characterized by hyperpigmentation that appears as symmetrical brown to grayish patches, and usually affects the facial region, however, few cases with extra facial involvement have been reported. The disease typically presents between the ages of 20 and 40 years with a strong female predominance, with reported ranges in male-to-female ratios between 4:1 and 39:1 [1]. Melanin is a biopolymer synthesized from amino acid tyrosine and is integral to pigmentation of the skin, hair, and eyes in mammals [2]. Melanogenesis refers to the formation of this pigment from specialized epidermal cells called melanocytes, which are also located in the hair follicles. Synthesized melanin is then packaged into organelles known as melanosomes [3,4]. Multiple melanosomes are then transported from melanocytes to neighboring keratinocytes, contributing to the skin pigmentation [5]. Melasma was previously considered a disorder primarily involving melanocytes, however, emerging evidence shows the significant contribution of dermal components, such as mast cells, solar elastosis, and neovascularization, in the pathogenesis of melasma. Chronic exposure to ultraviolet (UV) radiation induces persistent dermal inflammation, leading to the activation of fibroblasts [6]. These UV-stimulated fibroblasts secrete stem cell factor (SCF), which interacts with its receptor c-kit on epidermal melanocytes, thereby promoting melanogenesis [7]. Additionally, lesional skin in melasma demonstrates an increased presence of senescent fibroblasts compared to adjacent normal skin. These senescent cells are known to produce elevated levels of aging-associated proteins, including SCF, further contributing to melanogenic activity [8]. Molecular studies have also revealed dysregulation of the Wnt signaling pathway in melasma, characterized by increased expression of Wnt-associated modulators [9]. Concurrently, a decrease in Wnt inhibitory factor-1 (WIF-1) expression has been observed in hyperpigmented regions [10]. The reduced expression of WIF-1 in keratinocytes and fibroblasts is believed to enhance melanogenesis and facilitate melanosome transfer through activation of both canonical and non-canonical Wnt signaling pathways [10]. Furthermore, frizzled-related protein 2 (FRP2) has been identified as a promoter of melanogenesis via activation of the β-catenin signaling cascade [11]. In parallel, ultraviolet radiation-induced upregulation of cyclooxygenase-2 (COX-2) has also been implicated in stimulating melanocyte activity and contributing to increased pigmentation [12].

In the present study, we focused on the E3 ubiquitin-protein ligase UBR2 (UBR2) as a potential therapeutic target in melasma. This target was identified in our previous study through the analysis of microarray gene expression data obtained from the GEO database, employing a network biology-based approach [13]. Natural products have been widely used in the treatment of diverse skin diseases since ancient times due to their therapeutic effectiveness and low toxicity. To identify potential compounds, we focused on a library of phytochemicals derived from *Scutellaria baicalensis*, an herbal medicine with multiple pharmacological activities including antioxidant and anti-inflammatory properties and its role as a skin protective agent. The anti-melanogenic activity of several bioactive compounds derived from this plant has been reported in the literature [14]. We used in-silico drug discovery methods that comprised molecular docking based virtual screening with analysis of interactions to discover possible inhibitors of UBR2 and molecular dynamic simulation studies. Aiming at obtaining binding affinity, interaction stability and critical residue contribution of the target protein with its ligands, the phytochemical library of *Scutellaria baicalensis* was systematically screened through virtual screening method. Such a strategy allowed for the discovery of effective natural bioactive compounds that could be developed as an UBR2 inhibitor, which can serve the basis of subsequent experimental confirmation in melasma treatment.

Material and methods

Receptor Preparation

The three-dimensional crystal structures of the target protein E3 ubiquitin-protein ligase UBR2 (UBR2) was retrieved from the Protein Data Bank (PDB ID: 5TDA). The protein structure was pre-processed by removing all heteroatoms, co-crystallized ligands, ions and water molecules using PyMol[15] to prevent any interference during docking simulations. The bond angles were then optimized with energy minimization using Swiss-PDBViewer [16] to reflect a stable conformation that is likely the native biological state. This step is important for the docked results to reasonably represent protein-ligand interactions. We subsequently converted this minimized structure into the necessary format to allow for docking.

Phytochemical Library Preparation

A phytochemical library for Scutellaria baicalensis retrieved from IMPPAT 2.0, [17] a manually curated Indian herbal plant compound database. Total 57 phytochemicals derived from Scutellaria baicalensis plant were retrieved. The phytochemicals were prepared by correcting the ligand structure and optimizing its geometry. Each compound was subjected to checked to ensure stable conformers. Further phytochemicals were converted into docking-compatible formats (PDBQT), with proper assignment of charges and rotatable bonds. This preparation step is important to minimize docking errors and ensure the results are reproducible.

Molecular Docking

To study the binding affinity and interaction mechanisms between UBR2 with selected phytochemicals, molecular docking was performed using Auto Dock Vina [18]. Docking is an essential part of structure-based drug discovery that algorithmically predicts the favored pose of a ligand in the binding pocket of a target protein, which translates to information on binding strength and interaction mechanism. The PDBQT format files for both receptor and ligands were prepared. The grid box was centered on the entire UBR2 to include all residues. Docking was performed with sufficient exhaustiveness to capture reliable conformational sampling. Ligand binding was assessed using Auto Dock Vina, where each ligand was docked independently and binding affinities were computed based upon the scoring function implemented in Auto Dock Vina. Docking outcomes were ranked according to binding energy values, with more negative (lower) values corresponding with stronger binding interactions. Detailed interaction analysis was used to investigate the interaction mechanisms for phytochemicals, which could explain the stability of binding. The corresponding visualization and analysis were done using PyMol and Discovery Studio Visualizer [19], including hydrogen bonds, hydrophobic contacts, van der Waals, and pi-pi stacking interactions. These interactions are important for ligand specificity and the stability of the protein-ligand complex. Molecular docking is a relatively economic and efficient approach that allows for rapid screening of large libraries of possible compounds to identify potential lead molecules before experimental validation.

ADMET Analysis

In silico absorption, distribution, metabolism, excretion and toxicity (ADMET) analysis with pkCSM [20] and SwissADME [21] to further evaluate the drug-likeness and pharmacokinetic properties of identified phytochemicals. ADMET profiling should be performed early in the drug discovery process since many candidates with high binding affinity fail later due to poor

pharmacokinetics or toxicity. As a result, developing predictive models for ADMET properties facilitates the identification of compounds with an increased probability of clinical success. Pharmacokinetic parameters including intestinal absorption, distribution, cytochrome P450 interactions, clearance and toxicity endpoints were predicted in pkCSM tool. Physicochemical properties, lipophilicity, solubility, drug-likeness and Lipinski rule of five was evaluated by SwissADME. Compounds that exhibited favorable ADMET properties and had strong binding affinity along with stable interaction profiles were marked as potential candidates for further in vitro and in vivo validation.

Molecular Dynamics Simulations

Molecular dynamics simulations (MDS) were performed with the GROMACS 2022.4 package [22] to explore the structural stability and dynamic properties of apo UBR2 protein and their complexes with Ferulic acid and Skullcapflavone II. The CHARMM36 July 2022 force field [23] was utilized for protein parameterization, and the ligand topologies were created in CGenFF server to ensure compatibility with the chosen force field [24]. All systems were solvated in a cubic simulation box (using the TIP3P water model), and periodic boundary conditions were applied in all three dimensions. Relevant counter ions were also added to mimic physiological conditions in order to keep electrostatic neutrality. Before the simulation, each system was minimized by the steepest descent algorithm to remove steric clashes and obtain a stable conformation as an initial structure. Subsequent equilibration occurred in two distinct steps. The system was first equilibrated in NVT ensemble for the 500 ps to obtain stable temperature of 300 K followed by system equilibration under constant number of particles, pressure and NPT ensemble for 500 ps to attain stability while keeping at 1 bar, thereby permitting density adjustment. A suitable thermostat and barostat algorithms were used to couple temperature and pressure. After equilibration, a lengthy production run of 1000 ns (1 μs) was carried out for each system to sample the long-timescale conformational dynamics. Long-range electrostatic interactions were handled using the Particle Mesh Ewald method and bond constraints used LINCS algorithm to avoid numerical instability during simulation. Trajectory data were captured during the simulation and analyzed to evaluate structural stability/conformational behavior [25].

Principal Component Analysis

Principal component analysis (PCA) was used to investigate the collective movements and conformational dynamics of protein systems through simulation [26]. By condensing

trajectory data into a initial principal components that explain most of the structural variance, this technique allows to identify key motions [26]. Trajectories were aligned to a reference structure in order to discard translational and rotational movements, thus only internal motions were considered. Using the Cα atoms of the protein, a covariance matrix of atomic fluctuations was constructed and diagonalized to derive eigenvalues and eigenvectors. The direction in which it moves corresponds to the eigenvectors, while the magnitudes of these motions correspond to their eigenvalues. First few principal components were projected mainly PC1 and PC2 which are capturing greatest conformational fluctuations. Projected the trajectories onto these principal components to visualize conformational space explored throughout the simulation.

Free Energy Landscape Analysis

A free energy landscape analysis (FEL) based on the principal components from PCA was performed to gain additional insight into the conformational stability and transitions of the protein systems [27]. The free energy landscape gives an overview of the conformational states explored in the simulation by projecting the probability distribution of structures onto a reduced coordinate space spanned by its principal components. The first two principal components were used as collective variables to construct the free energy landscape in this study. The minima of energy landscape correspond to stable structural conformations that the protein samples during simulation, and higher energy regions represent unstable or less-explored states.

Result and Discussion

Molecular docking

Total 57 phytochemicals from Scutellaria baicalensis were retrieved from the IMPPAT 2.0 database and performed molecular docking against target protein UBR2. Auto Dock Vina was utilized to dock the compounds with the protein and predict docking affinity and interactions of each compound. The docking output provides binding affinities for the phytochemicals, in the range of -7.3 to -1.7 kcal/mol (Table 1). The stronger the binding affinity of compounds toward the UBR2 protein, the lower (more negative) their respective binding energy values. The docking studies indicated that certain phytochemicals achieved relatively high binding energies, suggesting their role as new UBR2 inhibitors. Apart from the binding energy, other parameters such as ligand efficiency, predicted inhibition constant (pKi) and torsional energy

were also analyzed using InstaDock tool. These parameters offered further understanding of how well the ligands were bound and correctly conformed. Ligand efficiency was calculated as a measure of binding per atom, with higher values being more favorable, pKi reflects the inhibition potential and favorable values. Torsional energy analysis also suggested that the flexibility of ligands in the binding pocket.

Such combined assessment of parameters like binding affinity, ligand efficiency, pKi and torsional energy enabled prioritization of crucial phytochemicals for further analysis. Our findings therefore highlight the potential of these Scutellaria baicalensis derived phytochemicals as candidate inhibitors of UBR2 and provide firm groundwork for further computational and experimental validation.

Table 1: Molecular docking results of phytochemicals against UBR2 showing binding energy, pKi, ligand efficiency, and torsional energy

S. No.	Phytochemicals identifier	Phytochemicals name	Binding Energy (kcal/mol)	pKi	Ligand Efficiency (kcal/mol/non-H atom)	Torsional Energy
1.	IMPHY004115	Baicalin	-7.3	5.35	0.2281	3.113
2.	IMPHY005607	Baicalein	-6.7	4.91	0.335	1.2452
3.	IMPHY009523	Skullcapflavone II	-6.3	4.62	0.2333	2.1791
4.	IMPHY005530	Wogonin	-6.2	4.55	0.2952	1.2452
5.	IMPHY004375	Skullcapflavone I	-6.2	4.55	0.2696	1.5565
6.	IMPHY014817	Aromadendrene	-5.6	4.11	0.3733	0
7.	IMPHY003977	(-)-beta-Bourbonene	-5.6	4.11	0.3733	0.3113
8.	IMPHY012168	(1S,2S,6S,7R,8R)-1,3-dimethyl-8-propan-2-yltricyclo[4.4.0.02,7]dec-3-ene	-5.6	4.11	0.3733	0.3113
9.	IMPHY011659	alpha-Muurolene	-5.5	4.03	0.3667	0.3113
10.	IMPHY014806	Caswell No. 264AB	-5.5	4.03	0.3667	0.3113
11.	IMPHY015123	alpha-Copaene	-5.5	4.03	0.3667	0.3113
12.	IMPHY011802	Ferulic acid	-5.5	4.03	0.3929	1.5565
13.	IMPHY003616	Bicyclogermacrene	-5.4	3.96	0.36	0
14.	IMPHY007376	beta-Cubebene	-5.4	3.96	0.36	0.3113
15.	IMPHY011957	(+)-delta-Cadinene	-5.4	3.96	0.36	0.3113
16.	IMPHY003720	(1S,6R,7R)-1-methyl-3-methylidene-8-propan-2-yltricyclo[4.4.0.02,7]decane	-5.3	3.89	0.3533	0.3113
17.	IMPHY011793	(+)-gamma-Cadinene	-5.3	3.89	0.3533	0.3113
18.	IMPHY011455	Cadina-1,4-diene	-5.3	3.89	0.3533	0.3113
19.	IMPHY011660	(+)-alpha-Cadinene	-5.3	3.89	0.3533	0.3113
20.	IMPHY011792	gamma-Muurolene	-5.3	3.89	0.3533	0.3113
21.	IMPHY014865	Calamenene	-5.3	3.89	0.3533	0.3113
22.	IMPHY011761	Humulene	-5.2	3.81	0.3467	0
23.	IMPHY014831	beta-Caryophyllene	-5.2	3.81	0.3467	0
24.	IMPHY011586	(S,1Z,6Z)-8-Isopropyl-1-	-5.2	3.81	0.3467	0.3113

		methyl-5-methylenecyclodeca-1,6-diene				
25	IMPHY016737	Methyl 2-methoxybenzoate	-4.7	3.45	0.3917	0.9339
26	IMPHY006269	(E)-4,8-Dimethyl-1,3,7-nonatriene	-4.6	3.37	0.4182	1.2452
27	IMPHY003050	Methyl salicylate	-4.5	3.3	0.4091	0.9339
28	IMPHY014835	(E)-beta-ocimene	-4.5	3.3	0.45	0.9339
29	IMPHY010072	Eucalyptol	-4.4	3.23	0.4	0
30	IMPHY011392	3-Carene	-4.4	3.23	0.44	0
31	IMPHY011599	Terpinolene	-4.4	3.23	0.44	0
32	IMPHY003982	gamma-Terpinene	-4.4	3.23	0.44	0.3113
33	IMPHY006145	p-Cymene	-4.4	3.23	0.44	0.3113
34	IMPHY014988	Limonene	-4.4	3.23	0.44	0.3113
35	IMPHY011789	Citral	-4.4	3.23	0.4	1.2452
36	IMPHY012061	alpha-Pinene	-4.3	3.15	0.43	0
37	IMPHY016217	2-(Methylamino)benzaldehyde	-4.3	3.15	0.43	0.6226
38	IMPHY012165	Sabinene	-4.2	3.08	0.42	0.3113
39	IMPHY011552	(1R)-2-methyl-5-propan-2-ylbicyclo[3.1.0]hex-2-ene	-4.1	3.01	0.41	0.3113
40	IMPHY005390	1-Octen-3-yl acetate	-4.1	3.01	0.3417	2.1791
41	IMPHY012097	Methyl octanoate	-4.1	3.01	0.3727	2.1791
42	IMPHY011804	cis-3-Hexenyl acetate	-3.9	2.86	0.39	1.5565
43	IMPHY007219	Isobutyl acetate	-3.6	2.64	0.45	0.9339
44	IMPHY002069	2-Methylbutyl acetate	-3.6	2.64	0.4	1.2452
45	IMPHY004121	2-Heptanone	-3.5	2.57	0.4375	1.2452
46	IMPHY007007	Ethyl isobutyrate	-3.4	2.49	0.425	0.9339
47	IMPHY012084	Sec-butyl acetate	-3.4	2.49	0.425	0.9339
48	IMPHY003179	3-Octanone	-3.4	2.49	0.3778	1.5565
49	IMPHY007171	1-Hexanol	-3.4	2.49	0.4857	1.5565
50	IMPHY001828	3-Octanol	-3.4	2.49	0.3778	1.8678
51	IMPHY004934	Tiglic aldehyde	-3.3	2.42	0.55	0.3113
52	IMPHY015730	3-Hexanol	-3.2	2.35	0.4571	1.2452
53	IMPHY003340	Acetoin	-3.1	2.27	0.5167	0.6226
54	IMPHY001971	1-Penten-3-OL	-3	2.2	0.5	0.9339
55	IMPHY007417	Ethyl acetate	-2.9	2.13	0.4833	0.6226
56	IMPHY007710	2-Butanol	-2.8	2.05	0.56	0.6226
57	IMPHY001846	Dimethyl disulfide	-1.7	1.25	0.425	0.3113

Interaction analysis

Interaction analysis of all phytochemicals with UBR2 showed that Ferulic acid and Skullcapflavone II, which were among the top-ranked phytochemicals, formed stable specific molecular interactions within same binding cavity (Fig.1). These interactions include hydrogen bonding, hydrophobic contacts, pi-interactions and van der Waals forces thus suggesting both ligands had a favorable accommodation within binding site region. Well-defined interaction network was observed for UBR2-Ferulic acid complex, which appeared to be primarily stabilized via the formation of multiple hydrogen bonds to residues THR141,

SER143 and PHE148. These hydrogen bonds are crucial for the stabilization of the ligand in the binding cavity. Other than hydrogen bonding, pi-sigma and pi-pi T-shaped interactions with THR109 and PHE103 respectively added to the stabilization via aromatic stacking interactions. Hydrophobic interactions such as alkyl/pi-alkyl contacts with VAL122 could improve the binding affinity by accommodating favorable nonpolar interactions in this pocket. In addition, many residues (THR120, GLY144, GLY146, GLY147 and ASP150) provided van der Waals interactions that along were holding up the ligand stabilization (Fig. 2A). Importantly, binding site analysis revealed that pivotal residues PHE148 and ASP150 located in the protein's L-arginine associated region suggesting Ferulic acid occupies a functionally relevant site within UBR2. The binding of UBR2-Skullcapflavone II complex inside the active site also exhibited strong and stable interactions, with GLY144, GLY145, and PHE148 hydrogen bonds were also observed while indicating a strong ligand anchorage. A pi-pi T-shaped interaction with the PHE148 residue tightly bound to the ligand with aromatic stacking as support, showing also that this residue plays a role in ligand recognition. Hydrophobic interactions alkyl/pi-alkyl contacts with VAL12 are another stabilizing factor for the complex. The interactions included numerous residues such as PHE103, THR109, THR120, THR141, THR142, SER143 and GLY146 and GLY147 which indicate extensive contact between the ligand and the protein surface (van der Waals contacts) (Fig. 2B). An analysis of binding revealed that PHE148 is central to ligand interaction in the region associated with L-arginine, indicating its importance as a key hot spot for interaction. Comparative analysis of the both complexes indicated similar interacting residues shared by both ligands PHE103, THR109, THR120, VAL122, THR141, SER143, GLY144, GLY146, GLY147 and PHE148 suggesting both ligands occupy a near-identical binding pocket within UBR2. Out of these residues, PHE148 repeatedly emerged as a vital residue that contributes to both hydrogen bonding and p-interaction, indicating its crucial contribution to ligand stabilization and recognition. The presence of common interaction residues further confirms the validity of docking results and suggests a conserved binding mechanism for these phytochemicals. In general, the interactions of Ferulic acid and Skullcapflavone II have a high binding affinity and fit well within UBR2 binding site. It offers a penitential to modulate UBR2 activity via hydrogen bonding, hydrophobic interactions, and aromatic stacking principles, thus providing a strong foundation for further studies.

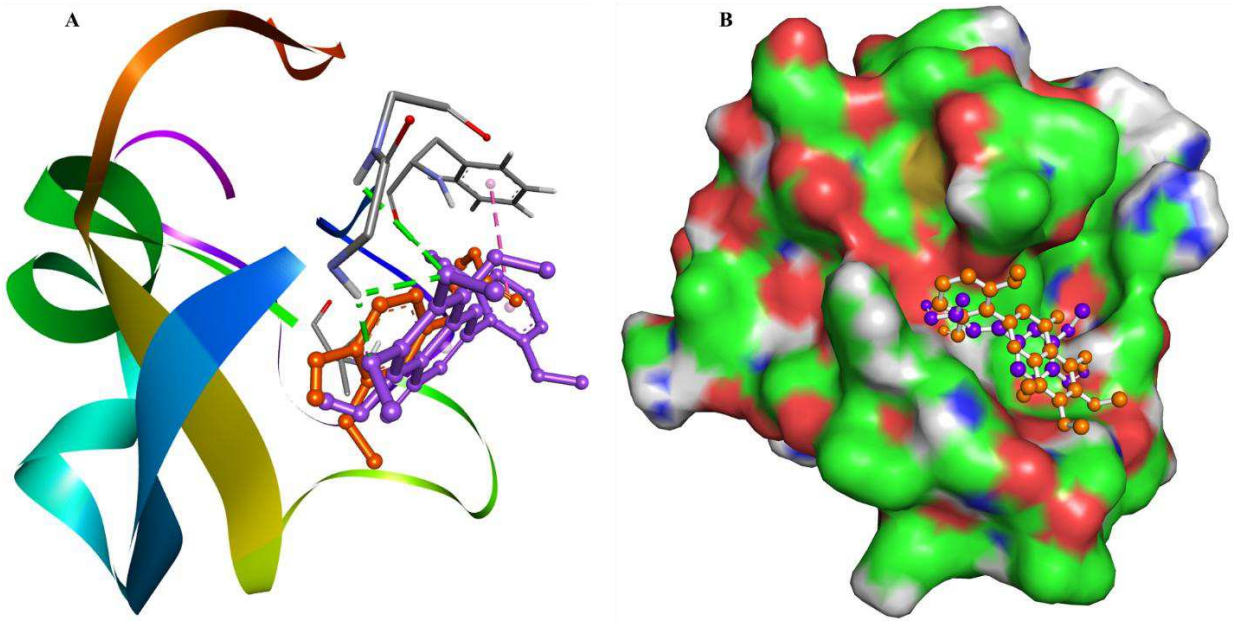


Fig. 1: A Cartoon view of UBR2 protein interacting with both ligands share similar binding cavities **B** Surface view of UBR2 protein with both ligands within similar binding cavity

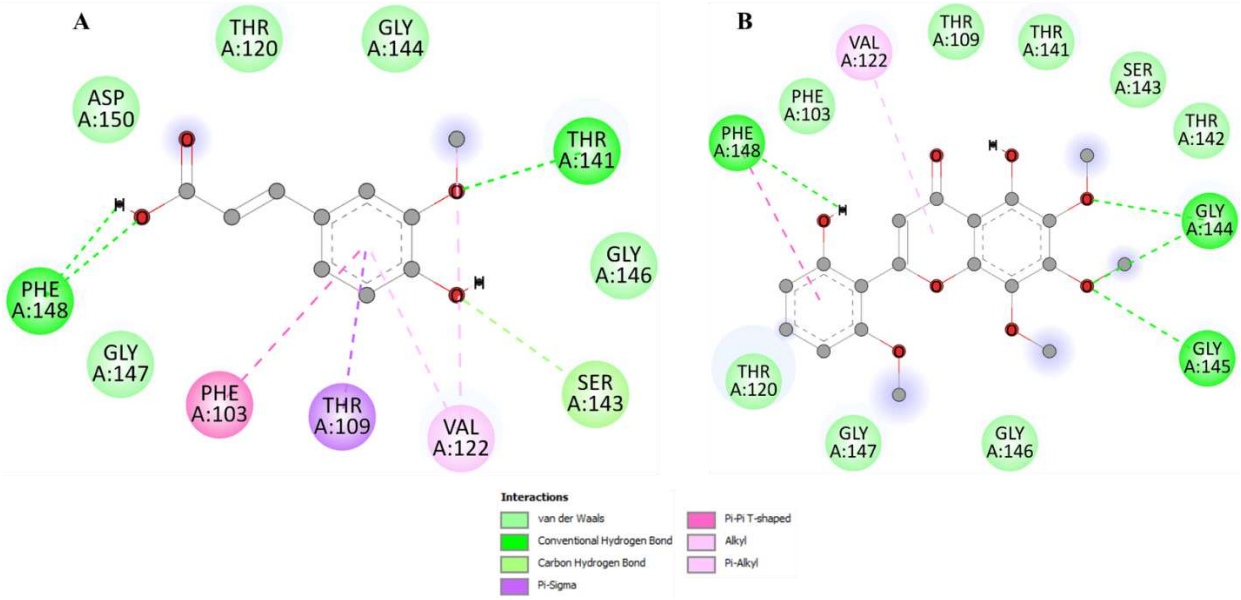


Fig. 2: A UBR2-Ferulic acid complex showing key interactions within the active site **B** UBR2-Skullcapflavone II complex illustrating binding orientation and interaction network

ADMET analysis

The pharmacokinetic and toxicity profile of selected phytochemicals Ferulic acid and Skullcapflavone II were evaluated to determine the drug-likeness and suitability as UBR2-targeting therapy. Both compounds showed acceptable physicochemical properties, fulfilling major drug-likeness rules (Lipinski, Ghose, Veber and Egan filters) without any violations.

Neither ligand displayed an alert in PAINS, suggesting minimal likelihood of interference with any assay therefore confirming their suitability as a drug candidate. Ferulic acid was found to have higher water solubility (-1.603 log mol/L) than Skullcapflavone II (-4.462 log mol/L), indicating a more favorable dissolution profile, considering its absorption properties. The intestinal absorption of both compounds was observed to be high, with Ferulic acid (Molecular Weight = 194.186) being slightly more absorbed (93.921%) than Skullcapflavone II (Molecular Weight= 374.345) (85.436%), suggesting good oral bioavailability (Table 2). Skin permeation profiling established similar values for both compounds, indicating moderate skin permeation potential. The distribution profile suggests moderate volume of distribution for both the compounds were mildly higher in its potential for distribution to different body compartments than Skullcapflavone II. In addition, the fraction of unbound drug for Ferulic acid was greater than Skullcapflavone II, indicating that the free active form is more likely to be available in systemic circulation and potentially improve its pharmacological activity. Both compounds were mentioned to be non-substrates of renal OCT2, making minor contributions to transporter-mediated renal excretion. Negative AMES toxicity predictions confirmed both Ferulic acid and Skullcapflavone II to be non-mutagenic. Moreover, neither of the compounds displayed evidence of hepatotoxicity or skin sensitization, further supporting their therapeutic index. In summary, the ADMET prediction indicates that both Ferulic acid and Skullcapflavone II could be promising candidates with favorable pharmacokinetic and safety properties. Compared to the two of them, Ferulic acid has better absorption, distribution and metabolic safety among them while Skullcapflavone showed acceptable drug-like characteristics with some limitations such as lower degree of solubility also potential inhibition for CYP1A2. Thus, they represent potential lead compounds for further validation through experiments against UBR2.

Table 2: ADMET properties of Ferulic acid and Skullcapflavone II including absorption, distribution, metabolism, excretion, and toxicity parameters

Pharmacokinetic Properties		**Ferulic acid**	**Skullcapflavone II**
Absorption	Water solubility (Numeric (log mol/L))	-1.603	-4.462
	Intestinal absorption (human) (Numeric (% Absorbed))	93.921	85.436
	Skin Permeability (Numeric (log Kp))	-2.881	-3.331
Distribution	VDss (human) (Numeric (log L/kg))	-0.851	-1.17
	Fraction unbound (human) (Numeric (Fu))	0.431	0.172
Metabolism	CYP2D6 substrate	No	No

	CYP2C19 inhibitor	No	No
	CYP1A2 inhibitor	No	Yes
Excretion	Total Clearance (Numeric (log ml/min/kg))	0.621	0.207
	Renal OCT2 substrate	No	No
Toxicity	AMES toxicity	No	No
	Hepatotoxicity	No	No
	Skin Sensitisation	No	No

Molecular dynamics simulations

RMSD and RMSF analysis

Root mean square deviation (RMSD) is an important metric that provides a measure of the overall structural stability of protein during MD simulations by quantifying deviation from initial conformation over time. Stability is indicated by lower and more stable RMSD values, while large fluctuations indicate conformational rearrangements. The RMSD profile of the apo UBR2 protein showed more variations throughout the simulation period, especially at both equilibration and mid-simulation stages, stabilizing 0.9-1.2 nm toward the end of simulations in this study. Both ligand-bound complexes exhibited relatively lower and stable RMSD trajectories, in sharp contrast (Fig. 3B). The UBR2-Ferulic acid formed cluster around 0.6-0.8 nm after equilibration, while for the UBR2-Skullcapflavone II complex showed even more stable RMSD, as they maintained the values around ~0.5-0.7 nm during most of the simulation time span (Fig. 3A). Distribution plots confirmed these observations, with the apo protein having a wider RMSD distribution, suggesting larger conformational diversity (Fig. 3D). Both complexes displayed more compact distributions indicative of lower structural dynamics. These findings are further supported by average of RMSD, where the RMSD mean value observed in apo UBR2 was higher than that for UBR2-Ferulic acid (0.70 nm) and UBR2-Skullcapflavone II (0.58 nm) (Table 3). Collectively, these results indicate that ligand binding stabilizes the UBR2 structure investigated in this study.

Root mean square fluctuations (RMSF) gives magnitude of the flexibility and dynamics of a protein at residue level during simulations. A larger RMSF value reflects greater flexibility of individual residues, while a smaller value indicates restricted motion and increased structure integrity. The residue-level fluctuation of apo UBR2 protein was greater than complex profile. On the other hand, ligand binding systems exhibited lower fluctuations across almost all residues, suggesting a stabilization upon ligands binding. Interestingly, key binding residues were observed to demonstrate decreased flexibility in the presence of ligands. Of

these complexes, UBR2-Skullcapflavone II displayed the least correlated movements of most residues, followed very closely by UBR2-Ferulic acid (Fig. 3B). High peaks of apo protein can be observed compared to the other curves, indicating higher flexibility from these regions. These observations are further supported by the distribution plots and average RMSF values, which show increased fluctuation of apo UBR2 (0.64 nm) compared to the UBR2-Ferulic acid (0.56 nm) and the UBR2-Skullcapflavone II complexes (0.53 nm) (Table 3). These results suggest that ligand occupancy locks localized flexibility, especially in functionally relevant regions impacting stabilization of structure.

Table 3: Average values of RMSD, RMSF, Rg, and SASA for UBR2 and its complexes

Complexes	RMSD (nm)	RMSF (nm)	Rg (nm)	SASA (nm)	Intra H-bonds
UBR2	0.95	0.64	1.39	61.7	25
UBR2-Ferulic acid	0.70	0.56	1.27	54.0	33
UBR2-Skullcapflavone II	0.58	0.53	1.27	54.9	31

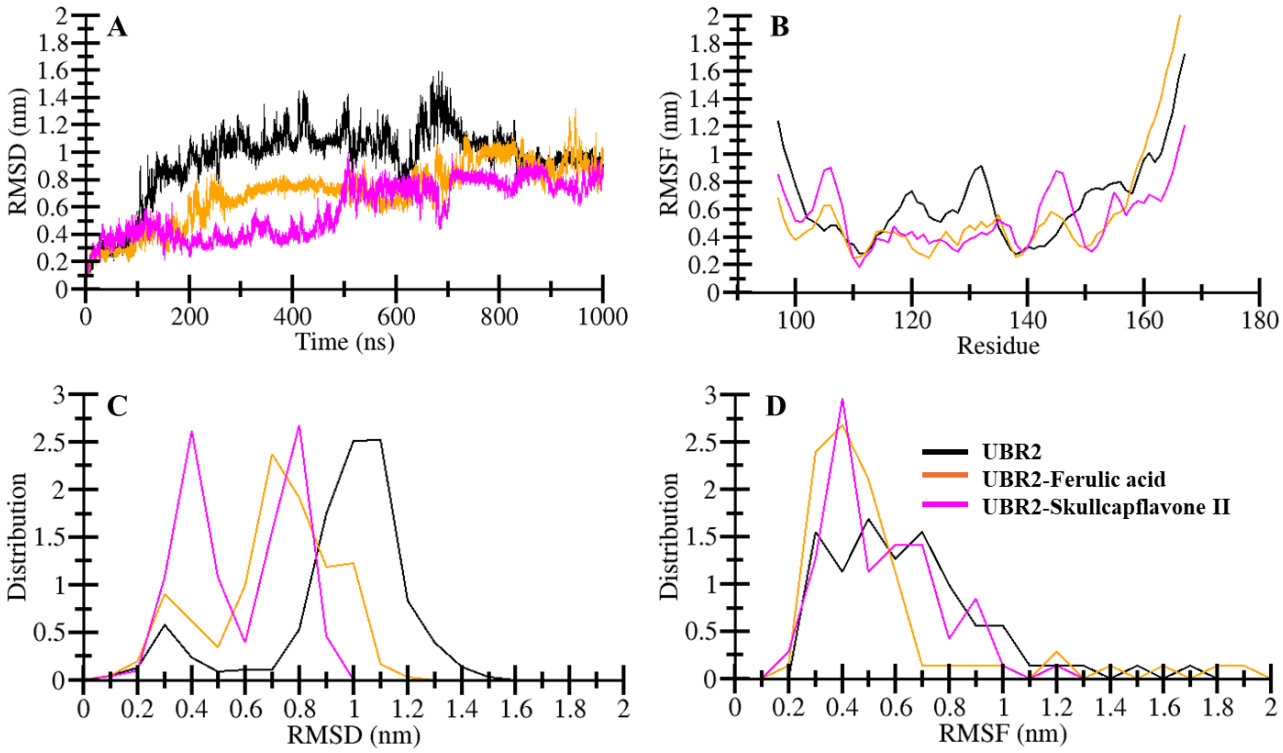


Fig. 3: A RMSD of UBR2, UBR2-Ferulic acid, and UBR2-Skullcapflavone II complexes over the simulation time, showing structural stability **B** RMSF per residue indicating flexibility differences between apo and ligand-bound systems **C** Distribution of RMSD values representing conformational variability **D** Distribution of RMSF values highlighting residue-level fluctuations

Rg and SASA analysis

The radius of gyration (Rg) is a measure of how compact the protein structure is during simulation. Generally, a lower and stable value of Rg represents a more compact and structurally stable protein, while higher or changing values represent structural expansion or instability. Rg trajectory of the apo UBR2 protein had significant fluctuations during the entire simulation, with occasional peaks representing an expansion of the protein structure. In the case of both ligand-bound complexes, lower Rg fluctuations over time indicated with a more stable profile (Fig. 4A). Complex UBR2-Ferulic acid and UBR2-Skullcapflavone II showed stable compactness throughout the simulation time, which suggested that ligand binding in general is beneficial for maintaining proper structural integrity during MD simulations. Apo protein sample a wider range of conformations, whereas the complexes exhibit narrower distributions reflecting the stabilized structural state (distribution plots) (Fig. 4C). The average Rg values of the UBR2 systems are 1.39 nm for apo UBR2, and 1.27 nm for both UBR2-Ferulic acid and UBR2-Skullcapflavone II complexes (Table 3). These findings indicate that ligand binding offers a more compact ancestral conformation, and both of the phytochemicals are comparable to transitions responsible for this structural compaction.

Solvent-accessible surface area (SASA) reflects the degree of protein solvent exposure, indicating folding and conformational reorientation as well as protein-ligand interactions. Lower SASA correlates with compactness and less solvent exposure. The SASA of the apo form UBR2 protein analysis revealed comparatively higher values and wider variations during simulation period indicating that there was a considerable exposure to solvent which would account for a very flexible nature of this structure (Fig. 4B). Conversely, ligand-bound complexes had lower SASA values with stable trajectories, suggesting decreased solvent exposure due to ligand binding. The SASA plots over time showed that both UBR2-Ferulic acid and UBR2-Skullcapflavone II complexes retained stable SASA values without too much deviation than the apo protein. This analysis provided further insight into the complexes, revealing a much narrower SASA range for occupancy to substantiate that these sets represent stable representative states. The average SASA values were 61.7 nm^2 for the apo UBR2 and lower for the complexes with UBR2-Ferulic acid (54.0 nm^2) and UBR2-Skullcapflavone II (54.9 nm^2) (Table 3). Further distribution plot also supports the SASA analysis (Fig. 4D). These observations suggest that ligand binding such as to still offers reduced solvent exposure and a more compact as well as stable protein structure.

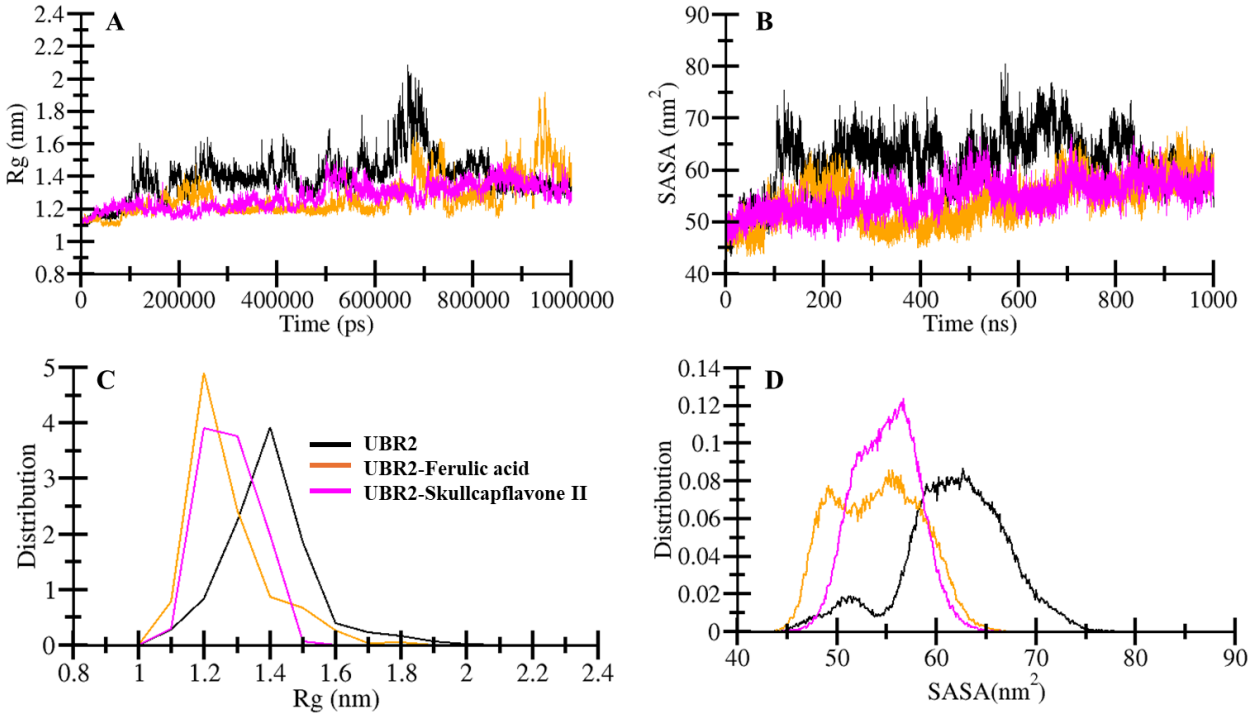


Fig. 4: A Rg of apo and ligand-bound systems over time, indicating structural compactness **B** SASA showing solvent exposure changes during simulation **C** Distribution of Rg values demonstrating compactness variations **D** Distribution of SASA values reflecting solvent accessibility differences

Hydrogen bonds analysis

The importance of intra-molecular hydrogen bonds in proteins during MD simulations is to maintain its structural integrity and internal stability. The stable and high number of intra-protein hydrogen bonds signifies a prominent secondary and tertiary protein structure, while major fluctuations suggest instability or conformational rearrangements. A calculation of time-dependent intra-molecular hydrogen bonds showed that the number of hydrogen bonds in the apo UBR2 protein overall fluctuates between 15 and 30 bonds on average during the simulation and is generally lower than for all other complexes. In comparison, the ligand-bound complexes had consistently higher numbers of intra-molecular hydrogen bonds with relatively stable profiles. The UBR2-Ferulic acid complex retained between 25 and 45 hydrogen bonds, while the UBR2-Skullcapflavone II complex was comparable but more stable at a range of 25 to 40 over the simulation time period (Fig. 5A). These observations are further supported by the distributions profiles whereby the apoprotein shows a narrower distribution centered at lower hydrogen bond counts, while the ligand-bound systems exhibit more broad distributions that have higher values (Fig. 5B). Apo UBR2 and the UBR2-Ferulic acid and UBR2-Skullcapflavone II complexes exhibited average intra-molecular hydrogen

bond counts of 25, 33, and 31, respectively (Table 3). These findings suggest that ligand binding enhances the internal hydrogen bonding network of the protein, promoting higher structural stability.

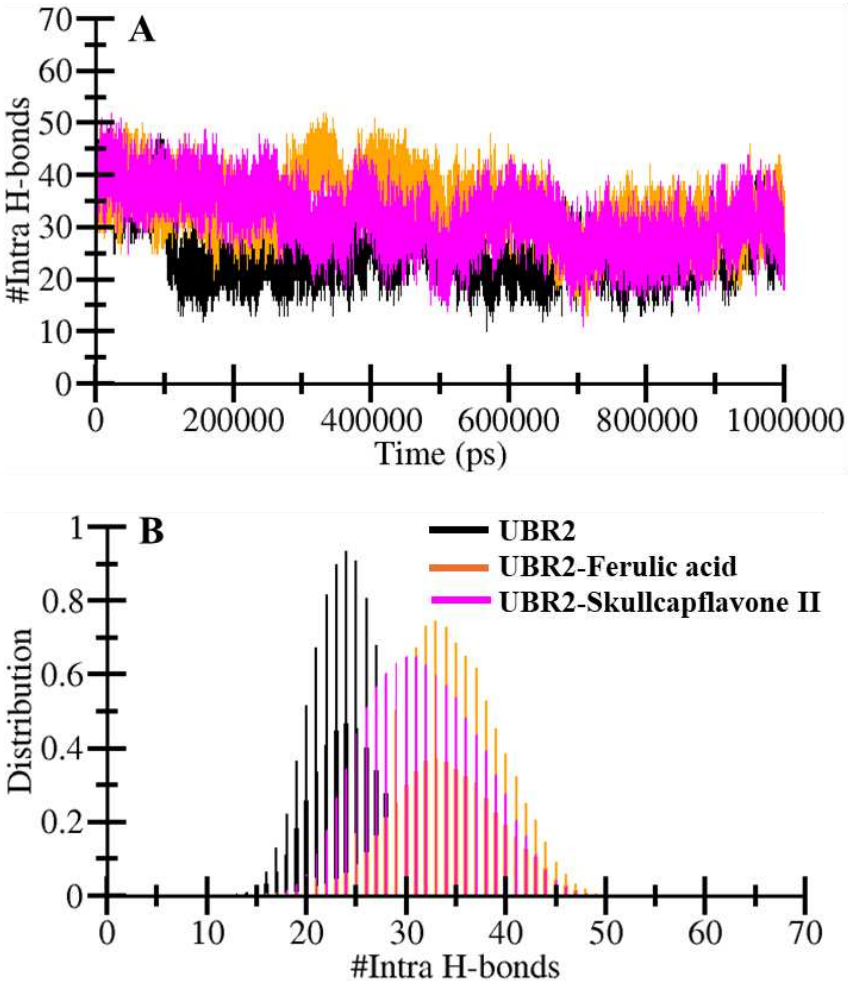


Fig. 5: A Intra-molecular hydrogen bonds in UBR2 and its complexes over simulation time **B** Distribution of intra-molecular hydrogen bonds

Inter-molecular hydrogen bonds formed between the protein and ligand are central to binding stability/specificity. These interactions drive the stability and lifetime of the protein-ligand complex, with stable hydrogen bonding over time being an indicator for stable ligand binding inside the active site. The time evolution of inter-molecular hydrogen bonds indicated that ligand-bound systems maintain persistent, hydrogen bond interactions with UBR2 over the course of simulation. The UBR2-Ferulic acid complex was primarily reasonably retaining 1-2 hydrogen bonds over time, with transient rises to around 3-4 bonds at some point suggestive of temporary strengthening of contacts within the binding pocket (Fig. 6A). Likewise, the UBR2-Skullcapflavone II complex showed a similar pattern in which ~1-2 hydrogen bonds were detected throughout the majority of the simulation with few peaks (up to 3-4) occurring

transiently (Fig. 6B). The distribution analysis further confirmed that the most likely number of inter-molecular hydrogen bonds for both complexes ranges from 1 to 2, which indicates that although multiple hydrogen bonds could be formed during ligand binding, only a small number of stable contacts are needed to maintain the ligands in receptors (Fig. 6C-D). However, both Ferulic acid and Skullcapflavone II showed stable binding via consistent inter-molecular hydrogen bonding with similar interaction patterns.

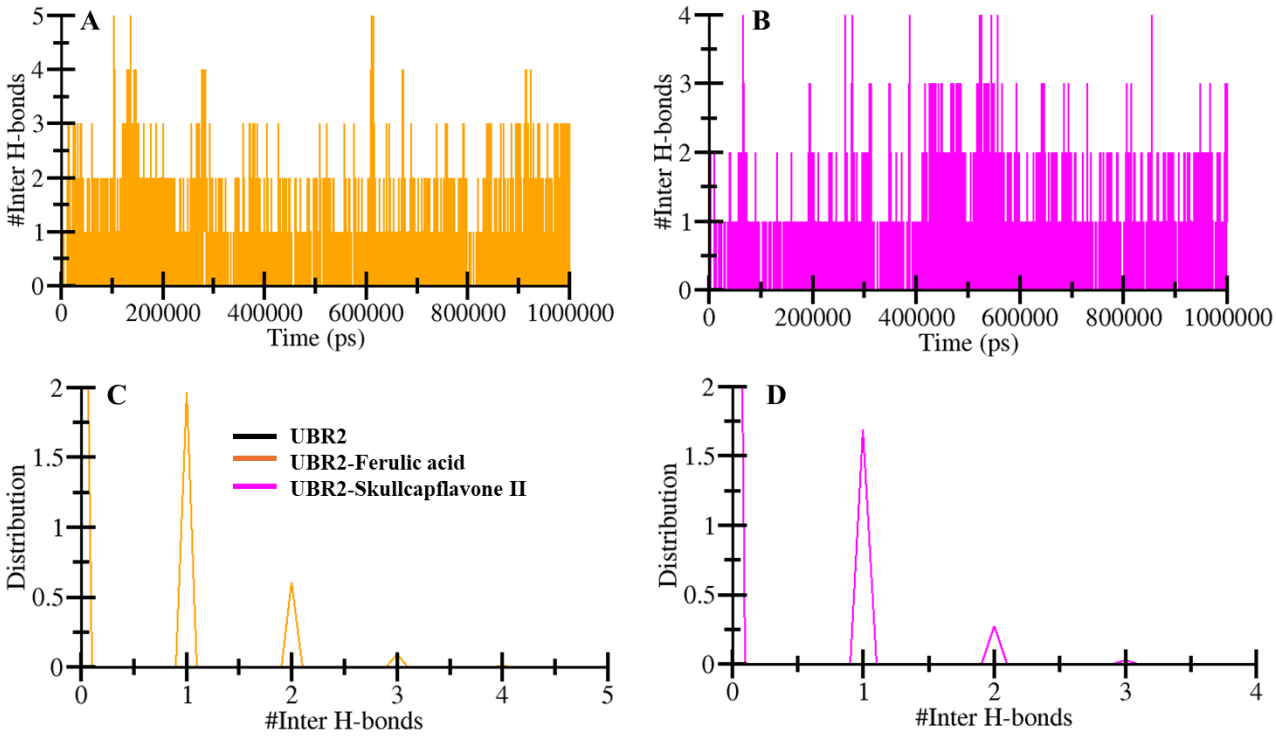


Fig. 6: A Inter-molecular hydrogen bonds in the UBR2-Ferulic acid complex over time **B** Inter-molecular hydrogen bonds in the UBR2-Skullcapflavone II complex over time **C** Distribution of Inter-molecular hydrogen bonds of UBR2-Ferulic **D** Distribution of Inter-molecular hydrogen bonds UBR2-Skullcapflavone II complex

Secondary structure analysis

Secondary structure analysis provides valuable information about the structural stability and conformational integrity of proteins during MD simulation. Differences in secondary structure elements, such as α-helices, β-sheets, turns and coils can illustrate protein folding, flexibility and the influence of ligand binding on overall structural organization. The time-dependent secondary structure snapshot also elucidated that apo UBR2 protein showed relatively more fluctuations within the structural elements across the simulation. Moderate variability for the total structured content (α-helix, β-sheet, β-bridge, and turns) suggests dynamic conformational transitions over time. The coil content was relatively higher in the

apo system, indicating greater structural flexibility. This is further confirmed by average proportions of structures as apo UBR2 stages 23 residues in structured areas and 28 residues having coil conformation with reasonable percentages from β-sheets (11 residues) and bends (13 residues). In contrast, ligand bound systems showed better structural organization with lower fluctuation in secondary structure elements. The UBR2-Ferulic acid complex demonstrated an increase in structured components with a total of 28 residues participating in the overall secondary structures. Importantly, β-sheet content increased to 15 residues and α-helical content increased to 5 residues compared to the apo protein. Simultaneously, it reduced to residues in coil content which shows a decrease in structural disorder. The time-dependent plot also shows fairly stable secondary structure elements during the simulation, even having less abrupt transitions compared to apo system. Analysis of Secondary Structure Retention in UBR2-Skullcapflavone II complex, similarly, the UBR2-Skullcapflavone II complex displayed stabilization of secondary structural elements retaining 28 structured residues throughout the simulation. The β-sheet content was slightly lower (9 residues) with a corresponding augmentation of turn (11 residues) and α-helical content (5 residues) (Fig. 7A-C). Its coil content was decreased by 25 residues compared to the apo one, implying less flexibility (Table 4). The profile of time-resolved secondary structure shows a more uniform accumulation of structural elements at this point, reflecting stable folding of the protein in the ligand interface. Overall, a comparative analysis of all systems suggests that binding to ligands helps stabilize the secondary structural elements and reduces coil regions while increasing ordered structures. Analysis reveals that both compounds contribute to preserving structural integrity. These results indicate that, upon ligand binding, the overall secondary structure transitions into a more stable and ordered conformation, with lower fluctuations compared to the apo UBR2 protein. Investigating dynamic parameters, these results align with the other findings and indicate the stabilizing effect of selected phytochemicals on UBR2 protein.

Table 4: Secondary structure composition of UBR2 and ligand-bound complexes during molecular dynamics simulation

Complexes	Structure	Coil	B-sheet	B-bridge	Bend	Turn	A-helix	5-helix	3-helix	PPII-helix
UBR2	23	28	11	1	13	9	1	0	0	4
UBR2-Ferulic acid	28	23	15	2	14	5	5	0	0	3
UBR2-Skullcapflavone II	28	25	9	2	11	11	5	1	1	3

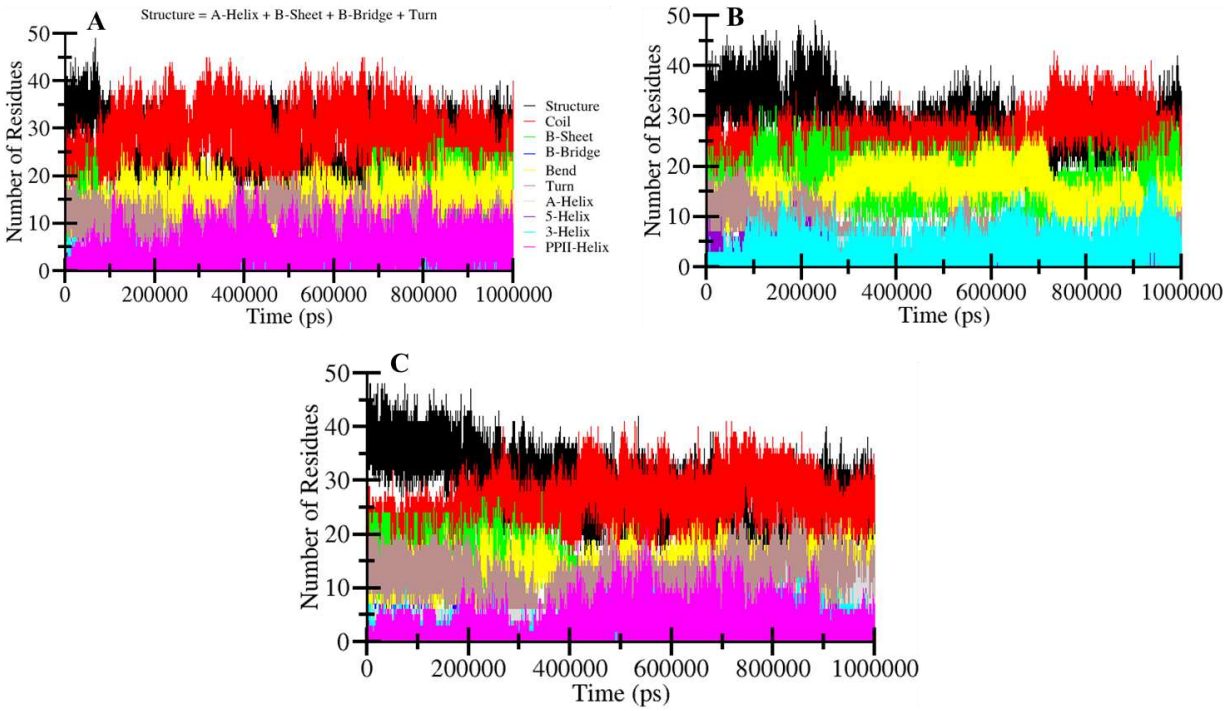


Fig. 7: Time evolution of secondary structural elements of UBR2 and its complexes during simulation **A** Apo UBR2 protein **B** UBR2-Ferulic acid complex **C** UBR2-Skullcapflavone II complex

PCA analysis

Principal component analysis (PCA), or essential dynamics, represents a versatile tool for identifying the dominant collective motions of a protein in MD simulations. PCA allows for systematic identification of large-scale, functionally relevant conformational changes through dimensionality reduction of atomic fluctuations into a few principal components. The contributions from first principal components (PC1) and second principal components (PC2) usually dominate the motion of the system, so they are informative of the conformational space sampled over the course of simulation. Perpendicular to each of the resulting projection trajectories along PC1 and PC2, marked differences in conformational sampling became evident between those states of apo UBR2 and analogous ligand binding poses. The apo UBR2 system occupied a broad and commonly dispersed conformational space, which is indicated by the significant span of points along both eigenvector axes. The broad nature of the distribution shows that the protein samples a plethora of dynamic conformations and structural states over this simulation, indicative of increased intrinsic flexibility. In comparison, the ligand-bound systems had relatively constrained conformational space. The UBR2-Ferulic acid complex displayed the restricted distribution, yet still sampling multiple

conformational regions indicating a partial restriction of the motional freedom of the protein upon binding. Interestingly, the UBR2-Skullcapflavone II complex was characterized by a much tighter and more defined cluster of conformations, suggesting an even greater attenuation of large-scale motions. Interestingly, the observed clustering pattern for this complex implies that in the presence of Skullcapflavone II a limited number of stable conformational states are adopted by the protein. Such observations are further corroborated by the time evolution of projections along PC1 and PC2. We observed that the apo protein was highly dynamic with time-dependent fluctuations further revealing interconversions among multiple conformational states. Compared to ligand-free, the systems with bound ligands showed a amplitude of motion and smoother transition especially in case of UBR2-Skullcapflavone II complex (Fig. 8A-D). This behavior suggests that ligand binding restrict enhances the dynamic behavior of the protein, which results in a stable population across conformational states. The overall reduction of dispersion evident in the PCA plots of the ligand bound systems, most prominently UBR2-Skullcapflavone II complex, indicates a stabilizing effect by ligands on protein structure. Conformational sampling is restricted, post-ligand binding, to favor stable conformations of UBR2 that are compatible with ligand-binding. These results agree with other dynamic parameters and strengthen the ability of the selected phytochemicals in stabilizing UBR2 protein.

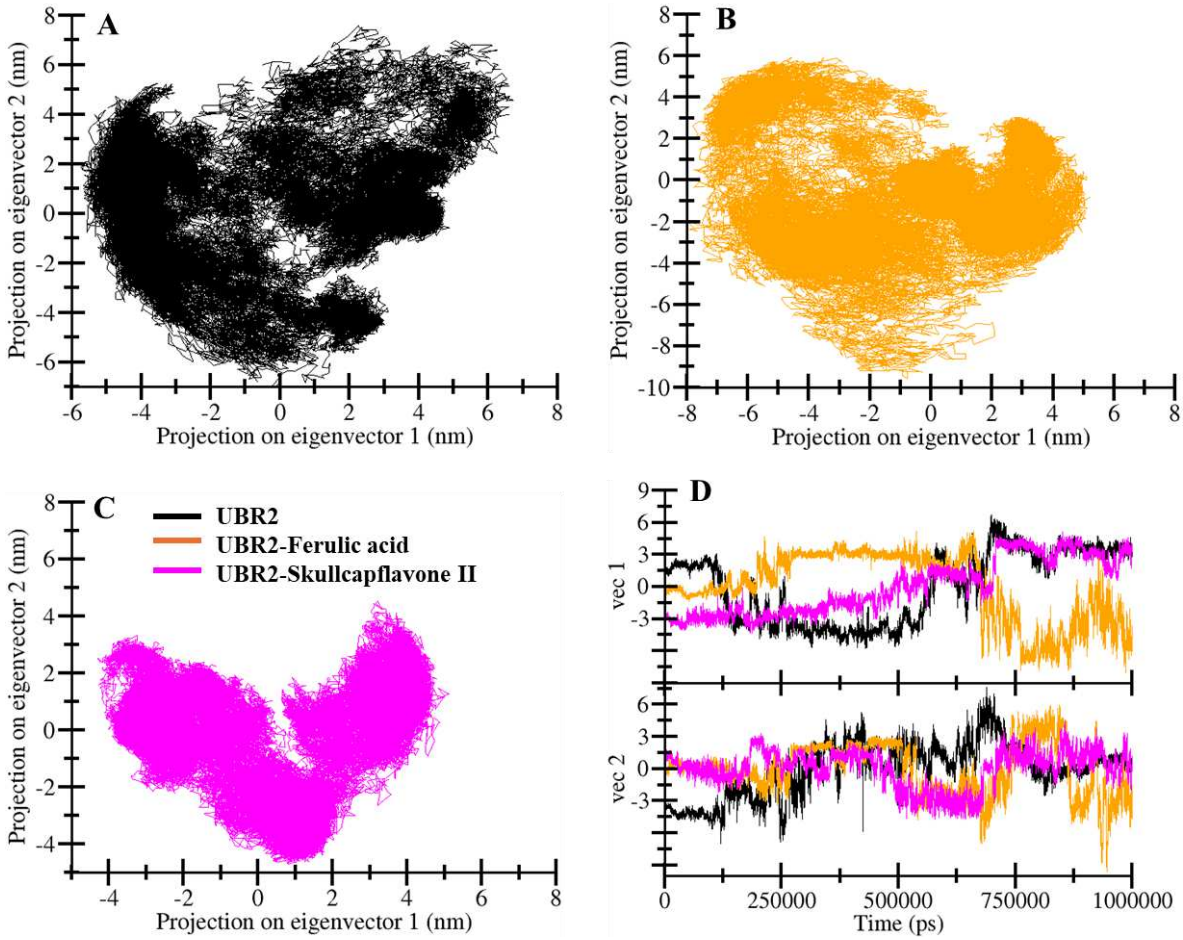


Fig. 8: Principal Component Analysis **A** Projection of apo UBR2 along PC1 and PC2 showing wide conformational sampling **B** Projection of UBR2-Ferulic acid complex indicating reduced conformational space **C** Projection of UBR2-Skullcapflavone II complex showing more compact clustering **D** Time evolution of principal components (PC1 and PC2) illustrating dynamic behavior during simulation

FEL analysis

The free energy landscape (FEL), a thermodynamically relevant view of conformational space visited by a protein in MD simulations, It can be understood in terms of energy as the minimization occurring at relatively low energies (low-energy regions), which refers to stable conformations (energy minima or basins) versus higher energy states, which are less likely and may correspond to transient or short-lived states. Hence, the number, depth and distribution of energy basins provide valuable information concerning protein stability and conformational transitions. The FEL of the apo UBR2 protein displayed a relatively broad and dispersed energy landscape with several shallow energy basins spread along PC1-PC2 space. This means that the apo consistent samples many conformational states and transitions between them occur on a rapid time scale. Finally, the presence of a number of low energy

conformations demonstrates conformational heterogeneity and relatively lower stability, since the protein does not become trapped into one dominant stable state. On the other hand, the ligand-free systems showed rather random energy landscapes while under the influence of ligands they were more organized. Compared to the apo protein, UBR2-Ferulic acid complex had less number but deeper energy wells. Instead, these basins were more localized, suggesting the protein settles into a small number of energetically favorable conformations when included with the ligand. However, a moderate degree of conformational flexibility was still observed as some spread in the landscape. Since the UBR2-Skullcapflavone II complex shows a much tighter and well-defined FEL with defined and deeper energy minima (Fig. 9A-C). As conformational states appeared more tightly clustered in certain areas within PC1-PC2 space, it also reflects a decreased base conformational variability. Longer-lasting, deeper basins indicate that the protein stays in stable conformations for a greater time span throughout the simulation period, which reflects improved thermodynamic stability. The three-dimensional FEL plots bolster these observations in that the apo protein shows a relatively rough surface exhibiting multiple shallow minima, whereas the ligand-bound systems most notably Skullcapflavone II features smoother landscapes with distinct energy wells (Fig. 10A-C). The diminished range and enhanced depth of the energy basins in the complexes suggest limited conformational sampling and stabilization of protein structure. Overall, the FEL analysis provides clear evidence that binding of ligand to UBR2 has an important influence on its conformational energy landscape. Ferulic acid and Skullcapflavone II both decrease conformational heterogeneity and increase energetically favorable states, we found a slightly stronger stabilizing effect of Skullcapflavone II over Ferulic acid. This is in agreement with PCA and other dynamic analyses, evident that ligand binding stabilizes the structure of UBR2.

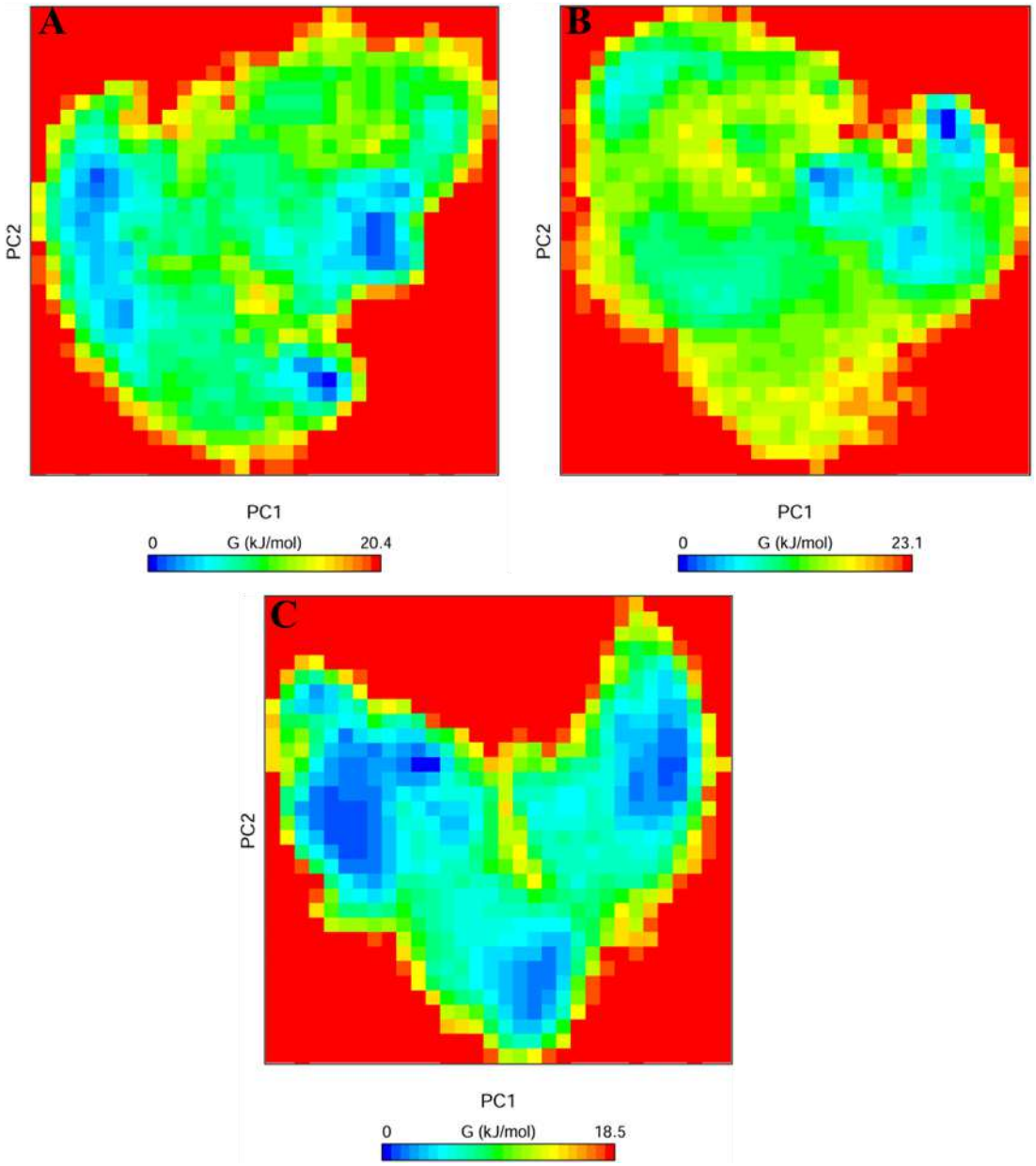


Fig. 9: Two-dimensional free energy landscapes of UBR2 and its complexes constructed using PC1 and PC2 as reaction coordinates **A** Apo UBR2 showing multiple shallow energy basins **B** UBR2-Ferulic acid complex showing more defined energy minima **C** UBR2-Skullcapflavone II complex showing deeper and more localized energy basins, indicating enhanced stability

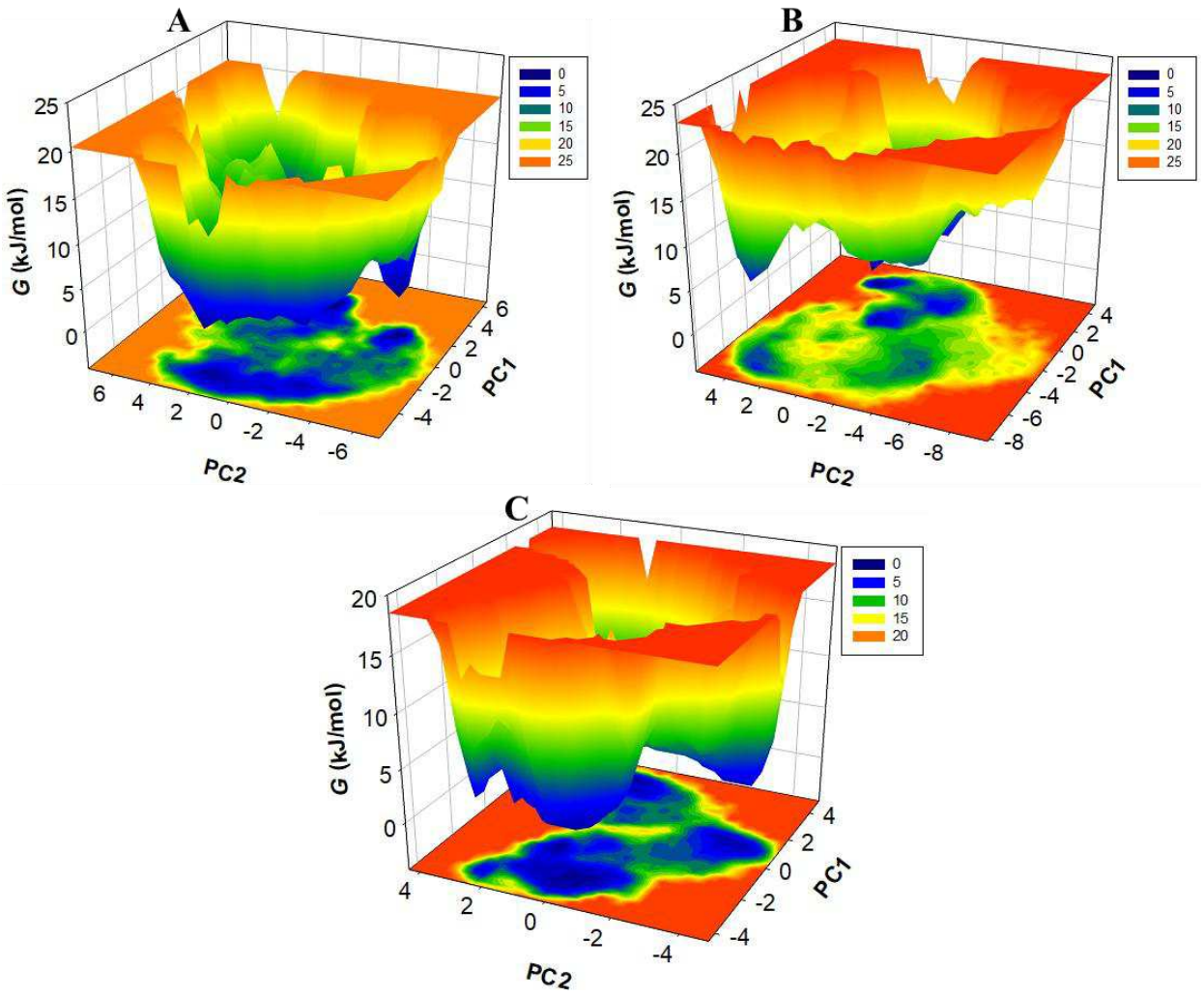


Fig. 10: Three-dimensional free energy landscapes of UBR2 and its complexes **A** Native UBR2 protein **B** UBR2-Ferulic acid complex **C** UBR2-Skullcapflavone II complex

Conclusion

In this study, an integrative in silico approach was employed to identify potential natural inhibitors of the E3 ubiquitin-protein ligase UBR2, a promising therapeutic target in melasma. Virtual screening of *Scutellaria baicalensis*-derived phytochemicals identified Ferulic acid and Skullcapflavone II as crucial candidates based on their binding affinity and interaction profiles. Both compounds demonstrated stable binding within a conserved active site, supported by key interactions involving critical residues such as PHE148. ADMET analysis confirmed favorable pharmacokinetic and safety properties, indicating their suitability as drug-like molecules. Long 1000 ns molecular dynamics simulations further revealed that ligand binding enhances the structural stability of UBR2 by reducing conformational fluctuations, increasing compactness, and stabilizing secondary structural

elements. Additionally, PCA and FEL analyses showed restricted conformational sampling and deeper energy minima in ligand-bound systems, indicating improved thermodynamic stability. Collectively, these findings suggest that Ferulic acid and Skullcapflavone II may serve as promising lead compounds targeting UBR2 in melasma. This study provides a comprehensive computational framework and a strong basis for future in vitro and in vivo validation to explore their therapeutic potential.

Acknowledgements

The authors Akhtar veg, Faria Saleem and Romana Ishrat wish to extend their appreciation to the Centre for Interdisciplinary Research in Basic Sciences (CIRBSc), Jamia Millia Islamia-110025 for providing the necessary research infrastructure.

Funding

No funding was received for conducting this study.

Ethical Approval

No ethical approval is required.

Author Contributions

Akhtar Veg: Conceptualization, Methodology, Data collection, Data analysis, Visualization, Validation, Writing-original draft and Editing; Faria Saleem: Conceptualization, Formal-analysis, Writing-review and Editing; Romana Ishrat: Supervision, Visualization, Writing-review and Editing.

Conflict of interest

The authors have no competing interests to declare that are relevant to the content of this article.

References

[1] I. Majid, S. Aleem, Melasma: Update on Epidemiology, Clinical Presentation, Assessment, and Scoring, J Skin Stem Cell 8 (2022). https://doi.org/10.5812/jssc.120283.

[2] M.E. McNamara, V. Rossi, T.S. Slater, C.S. Rogers, A.-L. Ducrest, S. Dubey, A. Roulin, Decoding the Evolution of Melanin in Vertebrates, Trends in Ecology & Evolution 36 (2021) 430–443. https://doi.org/10.1016/j.tree.2020.12.012.
[3] M. Cichorek, M. Wachulska, A. Stasiewicz, A. Tymińska, Skin melanocytes: biology and development, Pdia 1 (2013) 30–41. https://doi.org/10.5114/pdia.2013.33376.
[4] S. D'Mello, G. Finlay, B. Baguley, M. Askarian-Amiri, Signaling Pathways in Melanogenesis, IJMS 17 (2016) 1144. https://doi.org/10.3390/ijms17071144.
[5] M. Seiberg, Keratinocyte–Melanocyte Interactions During Melanosome Transfer, Pigment Cell Research 14 (2001) 236–242. https://doi.org/10.1034/j.1600-0749.2001.140402.x.
[6] S. Rajanala, M.B. de C. Maymone, N.A. Vashi, Melasma pathogenesis: a review of the latest research, pathological findings, and investigational therapies, Dermatol Online J 25 (2019) 13030/qt47b7r28c.
[7] H.Y. Kang, J.S. Hwang, J.Y. Lee, J.H. Ahn, J.-Y. Kim, E.-S. Lee, W.H. Kang, The dermal stem cell factor and c-kit are overexpressed in melasma: Dermal stem cell factor and c-kit in melasma, British Journal of Dermatology 154 (2006) 1094–1099. https://doi.org/10.1111/j.1365-2133.2006.07179.x.
[8] M. Kim, S.M. Kim, S. Kwon, T.J. Park, H.Y. Kang, Senescent fibroblasts in melasma pathophysiology, Experimental Dermatology 28 (2019) 719–722. https://doi.org/10.1111/exd.13814.
[9] H.Y. Kang, I. Suzuki, D.J. Lee, J. Ha, P. Reiniche, J. Aubert, S. Deret, D. Zugaj, J.J. Voegel, J.-P. Ortonne, Transcriptional Profiling Shows Altered Expression of Wnt Pathway– and Lipid Metabolism–Related Genes as Well as Melanogenesis-Related Genes in Melasma, Journal of Investigative Dermatology 131 (2011) 1692–1700. https://doi.org/10.1038/jid.2011.109.
[10] J.-Y. Kim, T.-R. Lee, A.-Y. Lee, Reduced WIF-1 Expression Stimulates Skin Hyperpigmentation in Patients with Melasma, Journal of Investigative Dermatology 133 (2013) 191–200. https://doi.org/10.1038/jid.2012.270.
[11] M. Kim, J.H. Han, J.-H. Kim, T.J. Park, H.Y. Kang, Secreted Frizzled-Related Protein 2 (sFRP2) Functions as a Melanogenic Stimulator; the Role of sFRP2 in UV-Induced Hyperpigmentary Disorders, Journal of Investigative Dermatology 136 (2016) 236–244. https://doi.org/10.1038/JID.2015.365.
[12] J.Y. Kim, J.Y. Shin, M.R. Kim, S. Hann, S.H. Oh, siRNA-mediated knock-down of COX-2 in melanocytes suppresses melanogenesis, Experimental Dermatology 21 (2012) 420–425. https://doi.org/10.1111/j.1600-0625.2012.01483.x.
[13] Centre for Interdisciplinary Research in Basic Sciences (CIRBSc), Jamia Millia Islamia, New Delhi-110025, India, A. Veg, M.M. Ahmed, Albert Einstein College of Medicine, Yeshiva University, New York City, R. Ali, Department of Biosciences, Jamia Millia Islamia, New Delhi-110025, India, R. Ishrat, Centre for Interdisciplinary Research in Basic Sciences (CIRBSc), Jamia Millia Islamia, New Delhi-110025, India, Identification of Hub genes in melasma using integrated transcriptomic analysis, Bioinformation 22 (2026) 1–8. https://doi.org/10.6026/973206300220001.
[14] L. Dai, L. Gu, K. Maeda, Inhibitory Effect and Mechanism of Scutellarein on Melanogenesis, Cosmetics 8 (2021) 15. https://doi.org/10.3390/cosmetics8010015.
[15] W.L. DeLano, Pymol: An open-source molecular graphics tool, CCP4 Newsl. Protein Crystallogr 40 (2002) 82–92.
[16] N. Guex, M.C. Peitsch, SWISS-MODEL and the Swiss-Pdb Viewer: An environment for comparative protein modeling, Electrophoresis 18 (1997) 2714–2723. https://doi.org/10.1002/elps.1150181505.

[17] R. Vivek-Ananth, K. Mohanraj, A.K. Sahoo, A. Samal, IMPPAT 2.0: an enhanced and expanded phytochemical atlas of Indian medicinal plants, ACS Omega 8 (2023) 8827–8845.
[18] O. Trott, A.J. Olson, AutoDock Vina: Improving the speed and accuracy of docking with a new scoring function, efficient optimization, and multithreading, J. Comput. Chem. (2009) NA-NA. https://doi.org/10.1002/jcc.21334.
[19] D. Studio, Discovery studio, Accelrys [2.1] (2008).
[20] D.E.V. Pires, T.L. Blundell, D.B. Ascher, pkCSM: Predicting Small-Molecule Pharmacokinetic and Toxicity Properties Using Graph-Based Signatures, J. Med. Chem. 58 (2015) 4066–4072. https://doi.org/10.1021/acs.jmedchem.5b00104.
[21] A. Daina, O. Michielin, V. Zoete, SwissADME: a free web tool to evaluate pharmacokinetics, drug-likeness and medicinal chemistry friendliness of small molecules, Sci Rep 7 (2017) 42717. https://doi.org/10.1038/srep42717.
[22] D. Van Der Spoel, E. Lindahl, B. Hess, G. Groenhof, A.E. Mark, H.J.C. Berendsen, GROMACS: Fast, flexible, and free, J Comput Chem 26 (2005) 1701–1718. https://doi.org/10.1002/jcc.20291.
[23] K. Vanommeslaeghe, E. Hatcher, C. Acharya, S. Kundu, S. Zhong, J. Shim, E. Darian, O. Guvench, P. Lopes, I. Vorobyov, A.D. Mackerell, CHARMM general force field: A force field for drug-like molecules compatible with the CHARMM all-atom additive biological force fields, J Comput Chem 31 (2010) 671–690. https://doi.org/10.1002/jcc.21367.
[24] K. Vanommeslaeghe, A.D. MacKerell, Automation of the CHARMM General Force Field (CGenFF) I: Bond Perception and Atom Typing, J. Chem. Inf. Model. 52 (2012) 3144–3154. https://doi.org/10.1021/ci300363c.
[25] R. Gargallo, P.H. Hünenberger, F.X. Avilés, B. Oliva, Molecular dynamics simulation of highly charged proteins: Comparison of the particle-particle particle-mesh and reaction field methods for the calculation of electrostatic interactions, Protein Science 12 (2003) 2161–2172. https://doi.org/10.1110/ps.03137003.
[26] G.G. Maisuradze, A. Liwo, H.A. Scheraga, Principal Component Analysis for Protein Folding Dynamics, Journal of Molecular Biology 385 (2009) 312–329. https://doi.org/10.1016/j.jmb.2008.10.018.
[27] A. Altis, M. Otten, P.H. Nguyen, R. Hegger, G. Stock, Construction of the free energy landscape of biomolecules via dihedral angle principal component analysis, The Journal of Chemical Physics 128 (2008) 245102. https://doi.org/10.1063/1.2945165.